The electronic structure of oxygen related defects in $PbWO_4$ and $CaMoO_4$ crystals

Yonas B. Abraham, N. A. W. Holzwarth,* R. T. Williams, and G. Eric Matthews
Department of Physics, Wake Forest University, Winston-Salem, NC 27109

Alan R. Tackett
Department of Physics and Astronomy, Vanderbilt University, Nashville, TN 37235

(Dated: September 11, 2001)

Several types of defect structures in $PbWO_4$ and $CaMoO_4$ are studied within the framework of density functional theory. While $PbWO_4$ is currently of greater technological interest, we were able to carry out more extensive calculations for $CaMoO_4$, including lattice relaxation, large simulation cells, and more complicated defects. The structural and chemical similarity of the two materials suggests that their defect properties may also be similar. The electronic structure of isolated oxygen vacancies, oxygen and Pb or Ca double vacancies, and substitutional Y are modeled using a supercell approximation. We find that the main effect of oxygen vacancies in $PbWO_4$ and $CaMoO_4$ is the introduction of states of W or Mo d character into the band gap. The energies of these defect states are very sensitive to their occupancy. An isolated O vacancy produces a doubly occupied defect state below the conduction band. Removing charge from this defect state lowers its energy and causes additional states of W or Mo d character to move into the band gap. Large supercell simulations for the Ca and O double vacancy in an unrelaxed or slightly relaxed structure, produce an unstable electronic structure suggesting the possibility of more extensive lattice distortion. In addition, we also present preliminary results of simulations of interstitial oxygen atoms in $CaMoO_4$, finding a relatively stable configuration with the interstitial O forming a weak bond between two MoO_4 clusters.

PACS numbers: 61.72.Ji,71.15.Nc,71.55.Ht,71.70.Ch

I. INTRODUCTION

Since the adoption of $PbWO_4$ single crystals as part of the scintillation detector system for the Large Hadron Collider at CERN[1, 2], there has been considerable interest in identifying possible defect structures in $PbWO_4$ and related crystals. These defects, which can affect the detector performance, may occur during crystal growth and also are likely to be produced by radiation during use. Lead tungstate and related materials have a long legacy of earlier work, some of which is described in References 3–7. New possible applications of these materials have recently been reported, including Cherenkov radiation production[8], high temperature ionic conductors[9], and Raman lasers[10].

There is a large literature of experimental work directed at identifying several types of defects in $PbWO_4$[11] and related materials. It is believed that Pb vacancies are often formed during the growth process. On the basis of X-ray and neutron diffraction, an ordered modification of $PbWO_4$ has been identified in which 1 out of every 16 Pb atoms are missing[12]. It is apparently difficult to directly control the stoichiometric concentration of Pb. However, it has been found that during the growth process, the addition of materials that can be incorporated as trivalent positive ions such as Y or La at the missing Pb sites can improve the luminescence properties of the resultant crystals[13, 14]. The direct observation of O vacancies is difficult, but spectroscopic studies of doped and annealed crystals indicate the presence of isolated oxygen vacancies and oxygen vacancies associated with cation vacancies[15–18]. In addition, studies of $PbWO_4$ crystals annealed in an oxygen atmosphere suggest that interstitial oxygen can also contribute to the defect structures[16, 17, 19, 20].

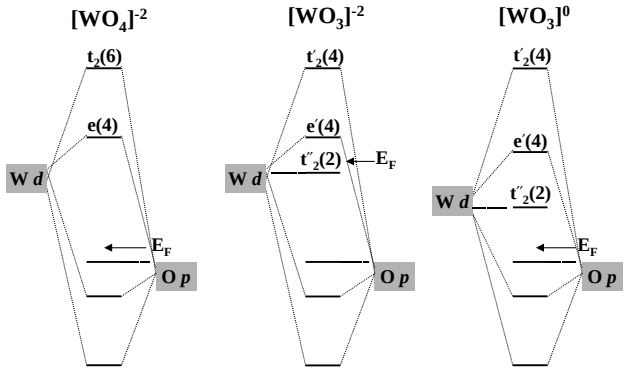

FIG. 1: Simplified molecular orbital diagram for states near band gap for $[WO_4]^{-2}$ (left panel), $[WO_3]^{-2}$ (middle panel), and $[WO_3]^0$ (right panel). The numbers in parentheses represent the degeneracy (including spin) of the orbital; "$\leftarrow E_F$" indicates the approximate location of the Fermi level. The $[WO_4]^{-2}$ group is found in the perfect crystal, while the other complexes represent possible defect configurations.

The purpose of this paper is to survey the electronic

* Corresponding author: natalie@wfu.edu; http://www.wfu.edu/~natalie

structures of some models of defects in $PbWO_4$ and $CaMoO_4$ in order to understand their ground state stability and qualitative electronic signatures. The calculations were performed within the framework of density functional theory[21, 22], using a supercell approach. Since density functional theory gives us a variational approximation to the electronic ground state of our defect models, we are able to estimate their energetics and optimal geometries. In addition, from partial densities of states, we obtain qualitative spectroscopic information. For technical reasons, we are able to carry out a more thorough investigation of $CaMoO_4$ than of $PbWO_4$. However, the structural and chemical similarity of the two materials suggests that their defect properties are likely to be similar.

Earlier electronic structure studies of perfect crystals of these materials[23] showed that states near the band gap are well described by a molecular orbital picture[24] of the anion group $[WO_4]^{-2}$. Here W (or Mo) is in an approximately tetrahedral site due to the four nearest neighbor oxygen ions and the group has a formal charge of -2. A simplified version of the molecular orbital diagram is presented in the left panel of Fig. 1, showing the occupied bands of mainly O p character well separated from the unoccupied bands of mainly W (or Mo) d character, split by the approximately tetrahedral crystal field and antibonding interactions into lower states of e symmetry and upper states of t_2 symmetry. Band gap defects could therefore be produced by changes to this anion group such as changes to its charge, geometry, and/or atomic constituents. In addition, since their crystal structure is not closely packed, additional atoms can be introduced into the lattice of these materials, and some of these can introduce new states into the band gap region.

For the purposes of describing the defect configurations simulated in this study we adopt the following notation in order to identify both the defect stoichiometry and the group dominating the states in the band gap:

$$\{\text{added atoms/removed atoms}\}\ [BO_n]^q. \qquad (1)$$

Here B represents the transition metal (only W or Mo in this study), n represents the number of coordinated O's (only 3 or 4 in this study), and q represents the net formal charge associated with the BO_n group. As we shall show, a simplified, although useful model of some of these effects are shown in the middle and left panels of Fig. 1.

The outline of the paper is as follows. In Section II, we describe the computational details of our simulations. In order to study the effects of geometry optimization in the vicinity of the defect site and to simulate large supercells, we used the *pwpaw* code[25] to study some model defects in $CaMoO_4$. In particular, the results of simulations of oxygen vacancies and interstitials, combined oxygen and Ca vacancies, and substitutional Y alone and in combination with O and Ca vacancies in $CaMoO_4$ are reported in Section III A. In order to extend some of these findings to $PbWO_4$, we used the WIEN97 code[26] which has been implemented for treating relativistic effects that better describe the heavy elements of Pb and W. In Section III B, we report results from our study of oxygen vacancies and combined oxygen and Pb vacancies in $PbWO_4$ simulated in an idealized geometry in a small supercell. Conclusions are given in Section IV, based on the comparison of the calculational results for $CaMoO_4$ and $PbWO_4$ and on the analysis of the more complete simulations for $CaMoO_4$.

II. CALCULATIONAL METHODS

A. Choice of supercells

The scheelite crystal structure is characterized by the body-centered tetragonal space group $I4_1/a$. In terms of the conventional unit cell parameters a and c, the following lattice vectors were used for the 2 formula unit simulations ("2x").

$$2\text{ unit}\begin{cases}\mathbf{A}_2 = \frac{1}{2}\left(-a\hat{\mathbf{x}} + a\hat{\mathbf{y}} + c\hat{\mathbf{z}}\right)\\ \mathbf{B}_2 = \frac{1}{2}\left(+a\hat{\mathbf{x}} - a\hat{\mathbf{y}} + c\hat{\mathbf{z}}\right)\\ \mathbf{C}_2 = \frac{1}{2}\left(+a\hat{\mathbf{x}} + a\hat{\mathbf{y}} - c\hat{\mathbf{z}}\right)\end{cases} \qquad (2)$$

This is, in fact, the same unit cell as the perfect crystal. The nearest distance between defects is a.

For the 8 formula unit simulations ("8x"), the lattice vectors were given by

$$8\text{ unit}\begin{cases}\mathbf{A}_8 = \left(a\hat{\mathbf{x}} + a\hat{\mathbf{y}}\right)\\ \mathbf{B}_8 = \left(a\hat{\mathbf{x}} - a\hat{\mathbf{y}}\right)\\ \mathbf{C}_8 = c\hat{\mathbf{z}}\end{cases}. \qquad (3)$$

The nearest distance between defects is $\sqrt{2}a$. Coincidentally, this 8 formula unit cell is the same unit cell recently analyzed[12] for the Pb deficient crystal having the stoichiometry $Pb_{7.5}W_8O_{32}$, with one of the Pb sites having $\frac{1}{2}$ occupancy.

For all of the simulations, the values of the lattice constants were taken from experiment and are listed in Table I.

TABLE I: Lattice constants used in the simulations.

Material	Ref.	a (Å)	c (Å)
$CaMoO_4$	27	5.222	11.425
$PbWO_4$	28	5.456	12.020

B. PAW calculations of $CaMoO_4$

In order to efficiently study the energetics and optimal geometry of the defects and to carry out simulations in large (8x) supercell, we used the *pwpaw* code[25, 29]

based on the projector augmented wave (PAW) approach of Blöchl[30] to study the non-relativistic material, $CaMoO_4$. The local density approximation (LDA) form of Perdew and Wang[31] was used to approximate the exchange-correlation interactions.

TABLE II: List of parameters used to construct basis and projector functions.

Atom	Z^a	nl basis	r_c^a (bohr)
O	8	$2s, \varepsilon s, 2p, \varepsilon p$	1.4
Ca	20	$3s, 4s, 3p, \varepsilon p, 3d$	1.9
Y	39	$4s, 5s, 4p, \varepsilon p, 4d, \varepsilon d$	1.9
Mo	42	$4s, 5s, 4p, \varepsilon p, 4d, \varepsilon d$	1.9

The first step of the PAW procedure is to produce the necessary projector and basis functions (analogous the construction of a pseudopotential function in a pseudopotential formalism). This is done using the *atompaw* code[32]. Since this material is both highly ionic and covalent, upper core electron states can be important for determining the self-consistent electronic structure. Specifically, we found it necessary to include projector and basis functions for the upper core states together with the valence states of Ca, Y, and Mo. The values of the local potential contributions $\tilde{v}^a_{\rm loc}(r)$ were constructed using the squared sinc shape function and aligned so that the pseudopotential basis functions corresponding to the valence s state of each atom are eigenstates of a purely local pseudo-Hamiltonian as described in Ref. 32. Table II lists the parameters used in this work. In this table, the notation ε indicates a continuum function, where the positive energy ε is chosen to ensure that the $\phi^a_{\varepsilon l}(r)$ basis function has the correct number of nodes in the augmentation region. For representing the valence $l = 1$ states of Ca, Y, and Mo, continuum basis functions $\phi^a_{\varepsilon p}$ were used instead of the bound ϕ^a_{4p} or ϕ^a_{5p} functions which had nodes inconveniently close to the augmentation radii. For O, in addition to the valence $\phi^{\rm O}_{2s}$ and $\phi^{\rm O}_{2p}$ functions, continuum basis functions $\phi^{\rm O}_{\varepsilon s}$ and $\phi^{\rm O}_{\varepsilon p}$ were also used to ensure that the negative ion states would be well-represented. In order to optimize the plane wave convergence, the augmentation radii r_c^a were chosen to be as large as possible without allowing the augmentation spheres to overlap. With this set of parameters, the reciprocal lattice cut off parameters could be taken to be 8 and 10 bohr^{-1} for the plane wave representations of the pseudowavefunctions $\tilde{\Psi}_{n\mathbf{k}}$ and the pseudodensity $\tilde{n}$, respectively.

During the course of the project, several other parameter sets were used, yielding similar results and demonstrating the expected insensitivity of the calculation to these parameters.

Both the 2x and 8x defect supercells were studied using the *pwpaw* code. For the 2x supercell, the Brillouin zone integrals were approximated by sampling 8 $\mathbf{k}-$points throughout the Brillouin zone. For the 8x supercell, the Brillouin zone integrals were approximated sampling only the zone center.

The partial densities of states were evaluated using a Gaussian smearing function[33] in the following form:

$$N^a(E) = \frac{2}{\sqrt{\pi}\sigma} \sum_{n\mathbf{k}} C^a_{n\mathbf{k}} \; W_{\mathbf{k}} \; {\rm e}^{-(E-E_{n\mathbf{k}})^2/\sigma^2}. \quad (4)$$

Here the factor of 2 comes form assuming that each distinct band is doubly occupied. The normalized Brillouin zone weight factors are denoted by $W_{\mathbf{k}}$. The band index is noted by n, and $E_{n\mathbf{k}}$ denotes the band energy. The coefficient $C^a_{n\mathbf{k}}$ represents the charge contained in a single sphere enclosing atom a, with radius taken to be the augmentation radius r_c^a, averaged over similar spheres. The Gaussian smearing parameter was taken to be $\sigma = 0.12$ eV.

For several of the defect systems studied, we were able to optimize the geometry of the atoms around the defect by moving the atoms within the supercell until the forces on them were smaller than a specified tolerance. In addition to obtaining the atomic positions of the optimized geometry, two energy measures could be determined. For each set of atomic positions $\{\mathbf{R^a}\}$, the *pwpaw* program calculates the LDA cohesive energy $E_{\rm coh}(\{\mathbf{R^a}\})$, defined to be the total electronic energy of the periodic system subtracted from the sum of the total electronic energies of the corresponding isolated spherical atoms. The "relaxation energy" measures the energy gained by geometry optimization, relative to the initial atomic positions $\{\mathbf{R^a_0}\}$, which, except for the missing atoms, were taken from perfect crystal positions:

$$\Delta E \equiv E_{\rm coh}(\{\mathbf{R^a}\}) - E_{\rm coh}(\{\mathbf{R^a_0}\}). \quad (5)$$

Also of interest, is an estimate of the formation energy for the defect, whose zero order approximation can be determined from the cohesive energy difference of the perfect and defective crystal simulations: $F^0 \equiv E_{\rm coh}({\rm crystal}) - E_{\rm coh}({\rm defect})$. Two corrections must be considered. First, since our defects involve oxygen, the final or initial state of the system involves molecular oxygen whose dissociation energy can be taken from the experimental value $D = 5.08$ eV[34]. Second, since the spherical atom approximation underestimates the total energy of each atom, the cohesive energies are generally overestimated. For the systems we are considering, these errors are negligible or cancel except for the total energy of one of the O atoms. An approximate correction can be determined from spectroscopic data[35, 36] which allows one to calculate the atomic ground state energy relative to the multiplet average which corresponds to the total energy calculated in the LDA results. For O, the multiplet correction energy can be estimated as $\Delta E_{\rm mult} \approx 0.94$ eV[36]. Therefore, the formation energies for *neutral* defects can be approximated as

$$F \approx F^0 \pm \left(\frac{1}{2}D + \Delta E_{\rm mult}\right) \approx F^0 \pm 3.48 \text{ eV}, \quad (6)$$

where the plus or minus signs pertain to interstitial O or O vacancies, respectively.

C. LAPW calculations of $PbWO_4$

For modeling defects in $PbWO_4$, where relativistic effects are important, we used the WIEN97 code[26] based on the linearized augmented plane wave (LAPW)[37] approach using the local density approximation (LDA) form of Perdew and Wang[31], as in the *pwpaw* calculations. The calculational parameters were taken to be the same as those used in our previous perfect crystal studies[23]. The defect simulations were performed using the 2x supercell only and the Brillouin zone integrals were approximated by sampling 27 $\mathbf{k}-$points throughout the Brillouin zone.[38] The partial densities of states were evaluated using Eq. 4, with the sphere radius chosen to be the muffin tin sphere radius[39]. The reason for switching codes for the $PbWO_4$ study is that relativistic effects, which have been not yet been implemented in the *pwpaw* code, are available WIEN97 code. In previous work[40, 41], we have shown that the PAW and LAPW methods produce essentially identical results for non-relativistic calculations.

III. RESULTS AND DISCUSSION

A. Defects in $CaMoO_4$

In order to study large simulation cells, atomic motions about the defect site, and more complicated defects, we carried out several calculations on $CaMoO_4$ which is structurally and chemically very similar to $PbWO_4$. For these simulations, the atomic positions of the perfect crystal were optimized, starting from the crystallographic results[27] finding the results listed in Table III. The calculated optimal Mo–O bond length is found to be slightly longer than the experimental value, as is typical of LDA calculations[42]. The calculated bond angles for Mo–O were found to be essentially identical to the experimental values. Table III also summarizes the geometry optimization results obtained for some of the defect simulations (using the notation defined in Eq. 1) which are discussed in the following subsections.

TABLE III: Geometry optimization results for ideal crystal and various defects in $CaMoO_4$. The experimental bond lengths and bond angles are quoted on the first line, in comparison with the calculated optimization results quoted on the second line. The remaining lines summarize the results of defect geometry optimizations using (2x) and (8x) supercells, listing the range of bond lengths and angles, the relaxation energies (ΔE) (Eq. 5), and formation energies (F) (Eq. 6).

System	Case	Mo-O bond lengths (Å)	Mo-O bond angles	ΔE (eV)	F (eV)
Ideal crystal	Exp.[a]	1.77	107^o, 114^o		
Ideal crystal	Cal.	1.79	107^o, 114^o		
$\{/O\}[MoO_3]^{-2}$	2x	1.79 – 1.83	105^o–117^o	0.2	7.1
$\{/O\}[MoO_3]^{-2}$	8x	1.79 – 1.81	106^o–115^o	0.2	7.1
$\{/CaO\}[MoO_3]^{0}$	2x	1.74 – 1.83	103^o–117^o	0.9	15.8
$\{O/\}[MoO_4]^{-2}$	2x	1.79 – 1.84	102^o–116^o	2.1	0.4

[a]Experimental X-ray results from Ref. 27.

O vacancy

The O vacancy ($\{/O\}[MoO_3]^{-2}$) was studied in both the 2x and 8x supercells. Table III summarizes the results of the geometry optimization. We see that the bond length and angular changes are similar but slightly larger for the 2x supercell compared with that for the 8x supercell. This is understandable since, in the latter case, the relaxation effects are spread over a larger number of sites. In both simulations, the relaxation effects are relatively small – the bond lengths increase by a few hundredths of an angstrom and the angles change by a few degrees, indicating that the $[MoO_3]^{-2}$ complex is relatively stable and structurally similar to the $[MoO_4]^{-2}$ complex from which it is derived. The calculated energy gained in optimizing the geometry was 0.2 eV and the formation energy for a neutral O vacancy was estimated using Eq. 6 to be 7.1 eV for both 2x and 8x simulations. The two simulations differed by less than 5% and 0.2% for the relaxation energies and formation energies respectively.

The partial densities of states for the 2x and 8x supercell simulations are compared with the partial densities of states of the perfect crystals in the top two panels of Figs. 2 and 3 respectively. The results for the two simulation cells look very similar to each other, with the main differences attributable to the effects of the different $\mathbf{k}$-point samplings of the supercell Brillouin zones. The bottom panel of Fig. 3 shows the partial densities of states for the unrelaxed geometry of the O vacancy in the 8x supercell. Comparison of the two lower panels (with and without geometry optimization) shows that changes in the partial densities of states due to lattice relaxation around the oxygen vacancy are very small. Similarly small lattice relaxation effects were found for the 2x simulation. These results suggest that the $\{/O\}[MoO_3]^{-2}$ defect in $CaMoO_4$ is rather insensitive to small geometry changes and that its effects are are spatially localized.

The partial density of states curves for the O vacancy show that an impurity state associated with the MoO_3 group is introduced below the conduction band. This state is fully occupied because the O vacancy removes 6 oxygen p states from the valence band while removing only 4 valence electrons, leaving 2 extra electrons which can be accommodated by the MoO_3 group – as described by the $\{/O\}[MoO_3]^{-2}$ notation.

In order to further characterize the defect state, it is helpful to examine the charge density contours. In Figs. 4 and 5, plots of charge density contours about the $[MoO_3]^{-2}$ site in a plane which contains an Mo-O bond and the missing O site, are shown for the 8x simulation. Fig. 4 is a plot for the uppermost occupied defect state near 2.2 eV. These contours illustrate the shape of a distorted Mo $4d$ orbital which has appreciable density in

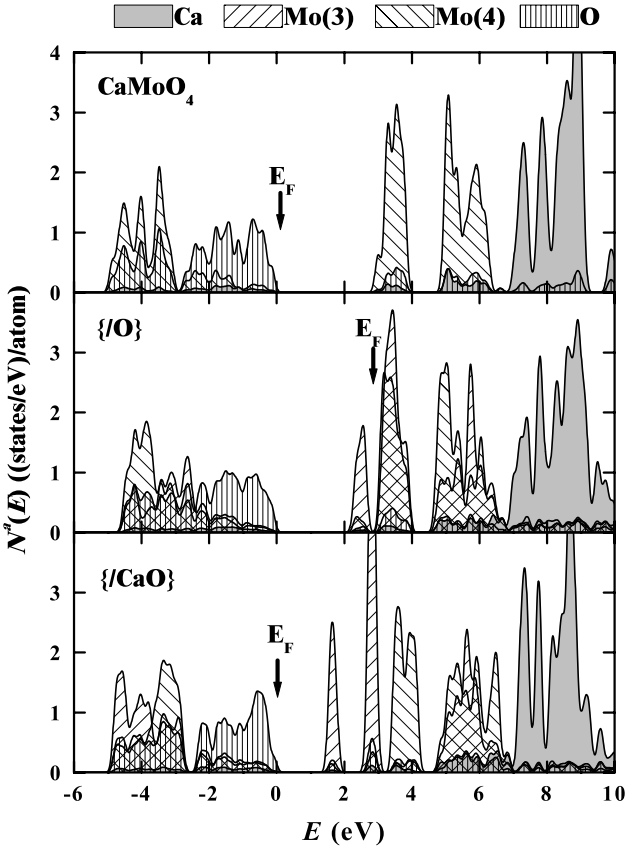

FIG. 2: Partial densities of states for 2x simulation of $CaMoO_4$: perfect crystal (top panel), O vacancy (middle panel), and Ca and O double vacancy (bottom panel). Calculations were done with lattice relaxation. The zero of energy for each plot is adjusted so that the top of the oxygen bands line up with that of the perfect crystal. For the defect plots, the two types of W sites – the 3-fold coordinated "(3)" and the 4-fold coordinated "(4)" are shaded differently. The Fermi level ("E_F") is indicated with an arrow in each plot.

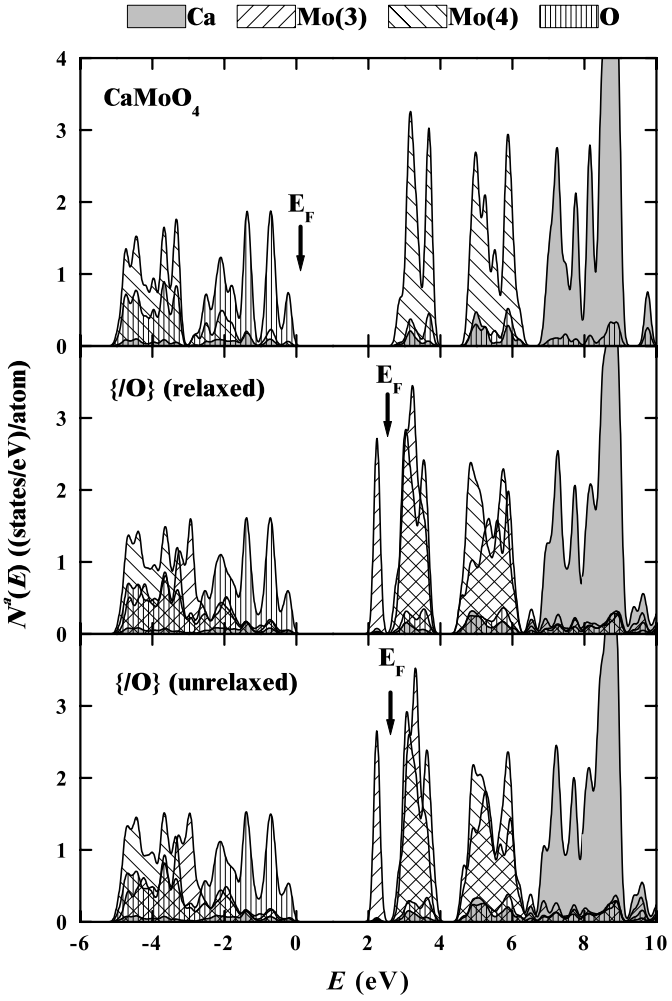

FIG. 3: Partial densities of states for 8x simulation $CaMoO_4$: perfect crystal (top panel) and O vacancy (middle panel),using the same notations as in Fig. 2. These calculations were done with lattice relaxation. For comparison, the bottom panel shows the partial density of states for the unrelaxed O vacancy.

the vicinity of the missing O and which we label "t_2''", for reasons discussed below. This picture is in marked contrast to that found for states associated with an oxygen vacancy in "simple" oxides such as MgO or CaO[43–45], which is usually called an "F-center". For the F-center, the electrons are confined by the electrostatic potential of the surrounding ions forming an $s-$like ground state[46], while for the $\{/O\}[MoO_3]^{-2}$ defect, the electrons occupy a Mo $4d$ orbital which is lowered in energy by the crystal field of the remaining oxygen ions.

Fig. 5 plots the charge density contours about the $[MoO_3]^{-2}$ site for the unoccupied states – (a) showing the lower conduction band between the energies 2.5-4.0 eV and (b) showing the upper conduction band starting above 4.0 eV. Since the partial density of states peaks for these two groups of states show (middle panel of in Fig. 3) comparable contributions from both the 3-fold and 4-fold Mo sites, it is not surprising that these two charge contour plots are similar to those of the perfect crystal[23], where the lower conduction band has e symmetry and the upper conduction band has t_2 symmetry. Also apparent in these plots are antibonding contributions from the nearest neighbor O $2p$-orbitals in the plotting plane.

The appearance of these 3 contour plots motivates us to analyze the $[BO_n]^q$ clusters in greater detail. For the perfect crystal[23], we showed that the $[BO_4]^{-2}$ cluster could be partially explained in terms of crystal field effects of the $O^{-\gamma}$ ions on the degenerate d states of W or Mo and partially in terms of hybridization between the W or Mo d states and the O $2p$, summarized by the molecular diagram shown in the left panel of Fig. 1. For the $[BO_3]^{-2}$ cluster, the crystal field effects can analyzed as follows. Idealizing the geometry of the cluster slightly so that $O^{-\gamma}$ ions are placed at 3 of the 4 ideal tetrahedral positions at a distance R from a central W or Mo ion, we

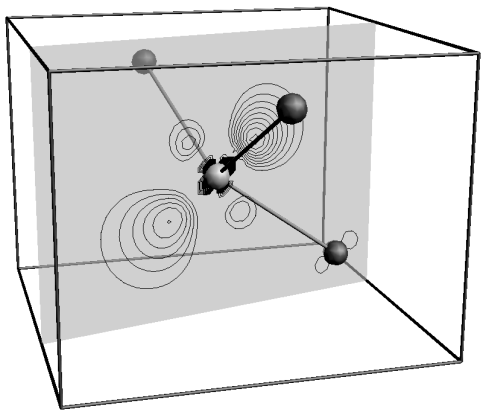

FIG. 4: Ball and stick model and contour plot for the 8x simulation of an O vacancy in $CaMoO_4$ at the $[MoO_3]^{-2}$ site. The plane on which the contours are draw passes through the Mo atom, one of it's nearest neighbor O atoms, and the plane of the O vacancy. The contour levels are drawn at intervals of 0.2 electrons/Å^3, with the lowest contour level at 0.2 electrons/Å^3 and represent the charge density of the occupied defect state.

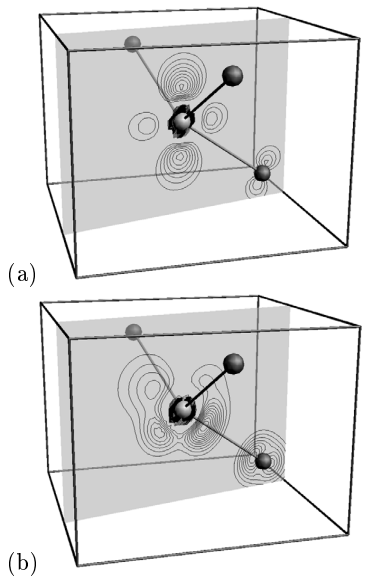

FIG. 5: Ball and stick model and contour plots for the 8x simulation of an O vacancy in $CaMoO_4$ at the $[MoO_3]^{-2}$ site similar to Fig. 4, but with contour levels representing the charge density associated (if the states had been fully occupied) with the unoccupied lower conduction band states(a) and upper conduction band states(b).

find that the leading term in the degenerate perturbation of the W or Mo d states can be written in the form:

$$\delta V_{mm'} = \frac{\gamma e^2 < r_d^2 >}{7R^3} M_{mm'}, \qquad (7)$$

where $M_{mm'}$ is a 5×5 matrix with indices m corresponding to the 5 azimuthal quantum numbers associated with the degenerate d ($l = 2$) states. Diagonalizing the matrix we find 3 eigenvalues:

$$\delta E = \frac{\gamma e^2 < r_d^2 >}{7R^3} \times \begin{cases} 2 & (2) & t_2' \\ -1 & (2) & e' \\ -2 & (1) & t_2'' \end{cases}, \qquad (8)$$

where the number in parenthesis denotes the degeneracy and the label on the right indicates the approximate relation to the corresponding state of pure tetrahedral symmetry. The lowest singly degenerate energy state which we have labeled "t_2''" has pure t_2 character. The two doubly degenerate states have mixed character, with slightly more e or t_2 character as indicated by the labels e' and t_2', resectively. We can estimate these energies for "B"=Mo, using $< r_d^2 > \approx 1$ Å, corresponding to the expectation value of the second power of the radius of the d orbitals of Mo (estimated from atomic orbitals), $R \approx 1.79$ Å corresponds to the Mo–O bond length, and $\gamma = 2$, we find the splitting between the extreme eigenvalues to be $\Delta E_{t_2'} - \Delta E_{t_2''} \approx 2.8$ eV. This is considerably larger than the corresponding crystal field splittings for tetrahedral geometry in the perfect crystal.[23] Interestingly, the partial densities of states for 3-fold coordinated W and Mo shown in figures 2, 3, and 9, as well as the charge density contour plots shown in Fig. 4 and 5 are consistent with this analysis in the sense that the self-consistent electronic structure of all of the defects containing $[BO_3]^{-2}$ clusters have 3 groups of states, the lowest state is occupied and has a single spatial degeneracy while the upper two states are unoccupied and have double spatial degeneracy. In addition to the crystal field analysis, hybridization of the d states of the B ion with the p states of O are also important in determining the electronic structure as illustrated in the middle panel of Fig. 1. Due to the spatial arrangement of the clusters, hybridization effects the t_2' states more than the others. Extending this analysis to the uncharged cluster $[BO_3]^0$, we might expect the energy diagram to be similar while the occupancies change as illustrated in the right most panel of Fig. 1. However, as we shall show below, the situation becomes considerably more complicated.

Ca and O double vacancy

Removing both Ca and O atoms changes the charge balance associated with the defect states since the missing Ca removes two valence electrons from the system. We expect that the double vacancy defect to be characterized by $\{/CaO\}[MoO_3]^0$ in our adopted notation. The results of the 2x simulation for the relaxed double vacancy are shown in the bottom panel of Fig. 2 for the partial density of states in Table III for the geometric and energetic results. The effects of geometry optimization are much larger than those of the single O vacancy, adjusting the energies of states associated with the $[MoO_3]^0$ clusters relative to other states of the system. Table III summarizes the relaxed Mo-O bond lengths and angles. In particular, we find that the Mo-O bond lengths associated with the $[MoO_3]^0$ groups to be shortened by 0.05 Å,

while those associated with the regular MoO_4^{-2} groups are approximately the same length as in the perfect crystal except for one bond which points in the direction of the missing oxygen which is lengthened by 0.04 Å. The simple description of this process is that the $[MoO_3]^0$ is able to compensate for the loss of charge by contracting its effective volume, thereby increasing the local charge density available for the Mo-O bonds. Correspondingly, the relaxation energy listed in Table III is much larger than for the single O vacancy case. The estimated formation energy is also listed in Table III.

While this explanation of the double vacancy seems reasonable, it apparently is not the whole story. Recognizing that the 2x simulation corresponds to an extremely high concentration of defects and that there are severe geometry restrictions consistent with the assumed supercell, we expect the results for the 8x simulation to be more reliable. Unfortunately, we have no results for the $\{/CaO\}[MoO_3]^0$ defect in the 8x simulation cell because we found it *impossible* to stabilize its self-consistency iterations with or without lattice relaxation effects. What appears to be happening in the more realistic simulation is that there is are two or more nearly degenerate configurations of this system. In addition to the $[MoO_3]^0([MoO_4]^{-2})_4$ configuration consistent with the 2x simulations, another configuration of the form $[MoO_3]^{-4\epsilon}([MoO_4]^{-2+\epsilon})_4$ seems to also exist. This second configuration corresponds to the partial transfer of negative charge (denoted by ϵ) to the $[MoO_3]^q$ group. This charge comes from the top of the O valence band and is presumably associated with the 4 nearest neighbor $[MoO_4]^{-2}$ groups. Apparently, the energy of the $[MoO_3]^q$ group is extremely sensitive to its charge state when q becomes less negative than $q = -2$, as confirmed by simulations with negatively charged supercells (compensated with a uniform positive charge).

Y substitutional and charge effects

In order to understand these charging effects in more detail and also to study the effects of trivalent substitutional impurities studied in the literature[14, 47], we performed some simulations with Y substituting for one of the Ca atoms ($\{Y/Ca\}[MoO_4]^{-(2+\delta)}$). Here δ represents the excess electronic charge incorporated into the lower conduction band due to the trivalent substitutional impurity Y. These calculations were done using the 8x supercell but without geometry optimization. Figure 6 (top panel) shows the partial density of states. The results show that Y adds electrons to the conduction band of $CaMoO_4$ and introduces new unnoccupied states primarily above the second conduction band, but introduces no new states of Y character within the band gap. This is similar to the behavior that we have found for $PbWO_4$:La simulations[48]. In future work, we hope to study the geometry relaxation of this system, in order to find out whether the model is consistent with the experimental observation that excess electrons can localize on one of the molybdate sites to form $[MoO_4]^{-3}$ centers. Recently, $[WO_4]^{-3}$ and $[WO_4]^{-3}$-La^{+3} centers have been identified in electron spin resonance studies of La doped $PbWO_4$ at low temperature[49, 50] with temperature dependences indicating binding energies of 0.05 and 0.27 eV, respectively below the conduction band energy.

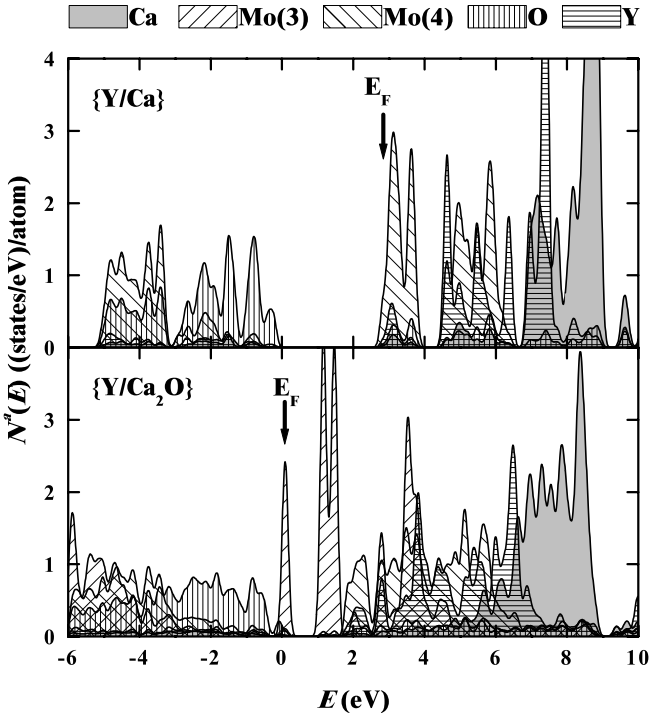

FIG. 6: Partial densities of states for 8x simulation $CaMoO_4$ with Y substituting for one Ca alone (top panel) and with a Ca and O vacancy double vacancy (lower panel),using the same notations as in Fig. 2 Calculations were done without lattice relaxation.

We also considered the effects of Y substitution impurities in conjunction with Ca and O double vacancies ($\{Y/Ca_2O\}[MoO_3]^{-1}$) using the 8x simulation cell without geometry optimization. The partial density of states are shown in the bottom panel of Fig. 6. Here we see that the extra charge from the trivalent Y is accommodated by the MoO_3 group. In contrast to the neutral CaO double vacancy, the excess charge from Y causes the $[MoO_3]^{-1}$ group to be electronically stable with a half-filled defect state (of "t_2'" character) just above the top of the valence band and an unfilled defect state (of "e'" character) below the conduction band.

Interstitial O

There is a fair amount of experimental evidence[18–20, 51] that interstitial oxygen can be accommodated into the $PbWO_4$ lattice. It is therefore of interest to study the corresponding defect in $CaMoO_4$. We have carried out a 2x simulation for an interstitial O atom initially placed between two Ca sites, and finding a stable O site between two MoO_4 groups. Figure 7 shows the optimized geometry with some of the bond lengths and angles listed

in Table III. As seen in the figure, the interstitial O forms a weak bond which bridges two oxygens associated with nearby $[MoO_4]^{-2}$ clusters. The O–O bond lengths are found to be 1.8 Å. Since we have not carried out an exhaustive geometry optimization, we believe there may be additional stable interstitial sites, such as found, for example in recent empirical potential simulations.[52] Table III also lists our calculated formation energy for the neutral interstitial O and finds it to be small (≈ 0.4 eV), suggesting that it could be relatively easy to introduce extra neutral O into this lattice.

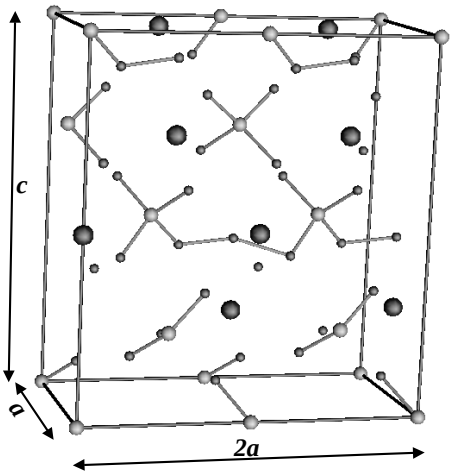

FIG. 7: Ball and stick model of stable configuration of interstitial O in CaMoO4 for 2x simulation. Atomic sites are shown with increasing sphere sizes in the order O, Mo, and Ca. Nearest neighbor Mo–O and O–O bonds are also indicated.

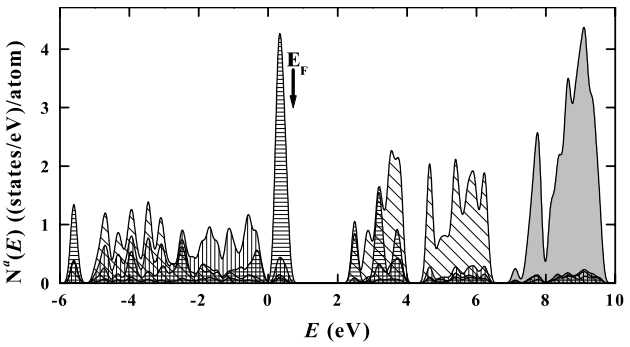

FIG. 8: Partial densities of states for 2x simulation of $CaMoO_4$ with an interstitial O atom, at the stable geometry shown in Fig. 7. The shadings of the various partial density of states curves is the same as in Fig. 2 except that the interstitial O states are indicated with horizontal stripes.

The partial density of states for our optimized geometry shown in Fig. (8) shows that interstitial O states are energetically aligned close to the O bands of the perfect lattice. By integrating the partial density of state curves in Fig. 8, we estimate that interstitial O's have a charge very similar to that the of tetrahedral O's. While formally the tetrahedral O's have a charge of $-2e$, molecular bonding reduces the actual charge.

Since the simulations were carried out for the 2x supercell, the concentration of extra O in the simulation corresponded to a stoichiometry of $CaMoO_{4.5}$. Experimentally, rather high concentrations of extra O has been achieved. For example, gravimetric analysis of $PbWO_4$ annealed in an oxygen atmosphere[19] suggests that it is possible to achieve a stoichiometry of $PbWO_{4.1}$, at least at high temperature.

B. Defects in $PbWO_4$

For the 2 formula unit simulations in $PbWO_4$, including those for the"perfect crystal", the atomic positions (except for those removed) were taken from the experimental crystallographic results[28] without allowing for optimization of the defect geometry. Two kinds of defects were modeled – an oxygen vacancy and a Pb and O double vacancy.

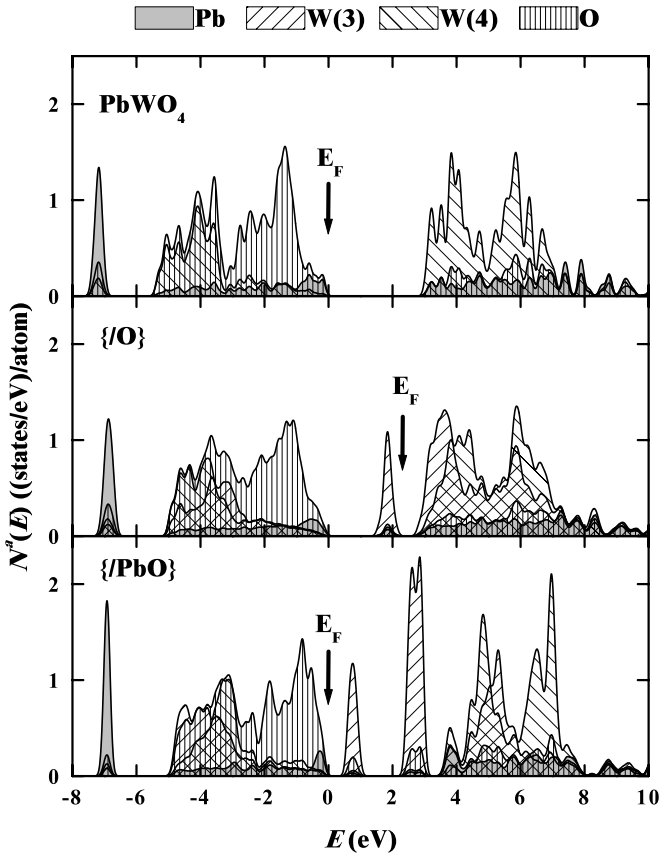

FIG. 9: Partial densities of states for $PbWO_4$, perfect crystal[39] (top panel), O vacancy (middle panel), and Pb and O double vacancy (bottom panel), using the same notations as in Fig. 2. Calculations were done without lattice relaxation.

In Fig. 9, the results for the partial densities of states

for the two defect simulations are compared with those of the perfect crystal. The results are very similar to the corresponding results for the 2x simulations of the $CaMoO_4$ system shown in Fig. 2. The main differences in the occupied states are that in $PbWO_4$ there is a narrow Pb $6s$ band at approximately 2 eV below the valence band and a corresponding anti-bonding contribution of of Pb $6s$ states at the top of the valence band. The main differences in the unoccupied states are that for $CaMoO_4$, the crystal field split Mo d states form two distinct bands of "e" and "t_2" character separated by nearly 1 eV. In $PbWO_4$, the crystal field split W d states of "e" and "t_2" character overlap, but form two distinct peaks. Also $PbWO_4$ lacks the equivalent of the high density of states at the top of the transition metal d states caused by the Ca $3d$ states in $CaMoO_4$.

What is of interest is the identification of defect states introduced into the band gap. Since we have such a high concentration of the defects, quantitative identification of the valence and conduction band edges are difficult. However, we can make the following qualitative analysis which is very similar to the $CaMoO_4$ case. For the O vacancy simulation, a peak associated with the 3-fold coordinated W site appears in the band gap, below the conduction band edge. This state is fully occupied because the O vacancy removes 6 oxygen p states from the valence band while removing only 4 valence electrons. Therefore, this defect would be given as $\{/O\}[WO_3]^{-2}$ in our suggested notation. The charge density contours associated with both the filled band gap state and the unfilled states in the conduction band are very similar to those shown in Figs. 4 and 5 for $CaMoO_4$. Since our $CaMoO_4$ simulations on the oxygen vacancy showed that our results were insensitive to supercell size and relaxation effects, we expect these results for the O vacancy in $PbWO_4$ to be similarly insensitive to supercell and relaxation effects.

For the Pb and O double vacancy, the partial density of states plot (bottom panel of Fig. 9) two peaks associated with the 3-fold coordinated W site appear in the band gap. These states are empty because the Pb vacancy does not remove any states from the valence band (other than from the narrow $6s$ band below the valence band), but removes 2 additional valence electrons. Thus this defect would be given as $\{/PbO\}[WO_3]^0$ in our suggested notation. Since our $CaMoO_4$ simulations on the Ca and O double vacancy could not be extended to the 8x supercell, we expect that the double vacancy in $PbWO_4$ to also be more complicated than implied by these unrelaxed 2x simulations.

IV. SUMMARY

These simulations of oxygen vacancies in $CaMoO_4$ and $PbWO_4$ focused attention on the ground state electronic structure of the $[BO_3]^q$ clusters. In addition to the electronic structure of the $[BO_3]^q$ clusters themselves, it is also important to understand the alignment of the cluster states with respect to the other states in the crystal. Our self-consistent calculations indicate that the $[BO_3]^q$ clusters are well defined and stable for $q = -2$ as found in the $\{/O\}$ simulations and is also stable for $q = -1$ as found in the $\{Y/Ca_2O\}$ simulations. For less negative values of q, the electronic balance between the $[BO_3]^q$ clusters associated with the O vacancy and the $[BO_4]^{-2}$ associated with the regular lattice seems to be very delicate.

In summary, we have shown that the main effect of O vacancies in $PbWO_4$ and $CaMoO_4$ is the introduction of states of W or Mo d character into the band gap. The energies of these defect states are very sensitive to their charge.

For a single O vacancy in $PbWO_4$ and $CaMoO_4$ ($\{/O\}[BO_3]^{-2}$), based on 2x and 8x simulations with relaxation effects included (for the $CaMoO_4$ case), we find a well-defined filled defect state below the conduction band, whose symmetry we have analyzed to be t_2'' with density contours shown in Fig. 4. This defect is very insensitive to lattice relaxation and simulation cell size. Since the state is completely filled, it cannot act as a trap for excess electrons. Furthermore, since its energy is approximately 0.7 eV below the conduction band minimum, it cannot be an effective electron donor. It might be be observable in infrared excitation, but cannot account for visible luminescence. If electrons are removed from the defect, we expect that its energy to be lowered and the spectrum to become more complicated.

For a PbO or CaO double vacancy in $PbWO_4$ or $CaMoO_4$ ($\{/AO\}[BO_3]^0$), based on 2x simulations, we find two groups of unfilled defect states within the band gap. The lower state is of t_2'' character, while the upper state is of e' character. Geometric optimization of the 2x $CaMoO_4$ simulation showed that shortened Mo–O bonds for the $[MoO_3]^0$ cluster are energetically favored. However, our inability to extend these calculations to the 8x supercell simulations suggests that this defect system is electronically metastable or perhaps unstable. Simulations with charged supercells and with substitutional Y described in Sec. III A show that the $[BO_3]^q$ defect is electronically stabilized with $q \leq -1$. In the absence of excess charge, such as provided by the substitutional trivalent Y atom, the lowest $[BO_3]^0$ state becomes degenerate with the O valence band. The fact that we are unable to stabilize this calculation has lead us to speculate that there are at least two nearly degenerate configurations of this system which we have described as involving the $[BO_3]$ site and its four nearest neighbor $[BO_4]$ sites in the form $[MoO_3]^0([MoO_4]^{-2})_4$ and $[MoO_3]^{-4\epsilon}([MoO_4]^{-2+\epsilon})_4$. This type of degeneracy usually results in a lattice distortion according to a Jahn-Teller mechanism[53]. This reasoning leads us to suggest that a CaO double vacancy may result in a more complicated defect, perhaps involving lattice distortions on several neighboring sites.

A single electron occupying an O vacancy in $PbWO_4$

has been suggested by Laguta and co-workers[54] as the model for a photo-induced "$Pb^+ - V_O$" center observed in electron spin resonance. The electron spin resonance signature is that of an electron interacting primarily with Pb nuclei adjacent the oxygen vacancy, and the authors refer to it as a Pb^+ center perturbed by a bare oxygen vacancy. The puzzle from the perspective of the calculations presented here is that the experiment finds little contribution from W $5d$ states. Laguta and co-workers suggest[54, 55] that there may be another lattice configuration of this defect, accessible over a thermal barrier, which resembles more closely an electron localized in an W $5d$ orbital. This second configuration may perhaps correspond to the $[WO_3]^{-1}$ center discussed in the present notation. This experiment and analysis suggests that lattice distortion may also be significant for the $q = -1$ defect. Further computational and experimental work is needed.

We have also presented preliminary simulations of interstitial neutral O introduced into the 2x lattice. These studies identified a possible stable site for the interstitial O and found the corresponding states to be near the crystalline O valence band. This preliminary work, suggests that further study of this system, including larger supercell simulations, charging effects, and perhaps simulation of dynamical effects, may be useful.

Missing from this work, is any information about the effects of these defects on luminescence. For this, it is necessary to go beyond the ground state density functional formalism, considered here.

ACKNOWLEDGMENTS

This work was supported by NSF grant DMR-9706575 and a SUR grant from IBM. We would like to thank Martin Nikl for very helpful comments.

[1] J. P. Peigneux, Nuclear Instruments and Methods in Physics Research A **351**, 197 (1994).
[2] P. Lecoq, I. Dafinei, E. Auffray, M. Schneegans, M. V. Korzhik, O. V. Missevitch, V. B. Pavlenko, A. A. Fedorov, A. N. Annenkov, V. L. Kostylev, et al., Nuclear Instruments and Methods In Physics Research Section A **365**, 291 (1995).
[3] F. A. Kröger, *Some Aspects of the Luminescence of Solids* (Elsevier Publishing Company. Inc., New York, 1948).
[4] W. V. Loo, Phys. Stat. Sol. (a) **28**, 228 (1975).
[5] R. Biederbick, G. Born, A. Hofstaetter, and A. Scharmann, Phys. Stat. Sol. (b) **69**, 55 (1975).
[6] R. Grasser, E. Pitt, A. Scharmann, and G. Zimmerer, Phys. Stat. Sol. (b) **69**, 359 (1975).
[7] A. Hofstaetter, R. Oeder, A. Scharmann, D. Schwabe, and B. Vitt, Phys. Stat. Sol. (b) **89**, 375 (1978).
[8] M. Kobayashi, S. Sugimoto, Y. Yoshimura, Y. Usuki, M. Ishii, N. Senguttuvan, K. Tanji, and M. Nikl, Nuclear Instruments and Methods in Physics Research A **459**, 482 (2001).
[9] T. Esaka, Solid State Ionics **136-137**, 1 (2000).
[10] A. A. Kaminskii, C. L. McCray, H. R. Lee, S. W. Lee, D. A. Temple, T. H. Chyba, W. D. Marsh, J. C. Barnes, A. N. Annanenkov, V. D. Legun, et al., Optics Communications **183**, 277 (2000).
[11] M. Nikl, Phys. Stat. Sol. (a) **178**, 595 (2000).
[12] J. M. Moreau, R. E. Gladyshevskii, P. Galez, J. P. Peigneux, and M. V. Korzhik, Journal of Alloys and Compounds **284**, 104 (1999).
[13] E. Auffray, P. Lecoq, M. Korzhik, A. Annenkov, O. Jarolimek, M. Nikl, S. Baccaro, A. Cecilia, M. Diemoz, and I. Dafinei, Nuclear Instruments and Methods in Physics Research A **402**, 75 (1998).
[14] M. Nikl, P. Boháček, E. Mihóková, M. Martini, F. Meinardi, A. Vedda, P. Fabeni, G. P. Pazzi, M. Kobayashi, M. Ishii, et al., Journal of Applied Physics **87**, 4243 (2000).
[15] A. N. Annenkov, A. A. Fedorov, P. Galez, V. A. Kachanov, M. V. Korzhik, V. D. Ligun, J. M. Moreau, V. N. Negedov, V. B. Palenko, J. P. Peigneux, et al., Phys. Stat. Sol. (a) **156**, 493 (1996).
[16] M. Nikl, K. Nitsch, J. Hybler, J. Chval, and P. Reiche, Phys. Stat. Sol. (b) **196**, K7 (1996).
[17] M. Nikl, K. Nitsch, S. Baccaro, A. Cecilia, M. Montecchi, B. Borgia, I. Dafinei, M. Diemoz, M. Martini, E. Rosetta, et al., Journal of Applied Physics **82**, 5758 (1997).
[18] A. Annenkov, E. Auffray, M. Korzhik, P. Lecoq, and J. P. Peigneux, Phy. Stat. Sol. (a) **170**, 47 (1998).
[19] W. Li, T. B. Tang, and X. Feng, Journal of Applied Physics **87**, 7692 (2000).
[20] C. Shi, Y. Wei, Z. Yang, D. Zhou, C. Guo, J. Liao, and H. Tang, Chemical Physics Letters **328**, 1 (2000).
[21] P. Hohenberg and W. Kohn, Physical Review **136**, B864 (1964).
[22] W. Kohn and L. J. Sham, Physical Review **140**, A1133 (1965).
[23] Y. Zhang, N. A. W. Holzwarth, and R. T. Williams, Phys. Rev. B **57**, 12738 (1998).
[24] C. J. Ballhausen and A. D. Liehr, Journal of Molecular Spectroscopy **2**, 342 (1958).
[25] A. R. Tackett, N. A. W. Holzwarth, and G. E. Matthews, Computer Physics Communications **135**, 348 (2001).
[26] P. Blaha, K. Schwarz, and J. Luitz, **WIEN97**(Improved and updated Unix version of the original copyrighted WIEN-code, which was published by P. Blaha, I. Schwarz, P. Sorantin, and S. B. Trickey, in *Comput. Phys. Commun.* **59**, 399 (1990.)), Tech. Rep., Vienna University of Technology (1997).
[27] R. M. Hazen, L. W. Finger, and J. W. E. Mariathasan, J. Phys. Chem. Solids **46**, 253 (1985).
[28] J. M. Moreau, P. Galez, J. P. Peigneux, and M. V. Korzhik, Journal of Alloys and Compounds **238**, 46 (1996).
[29] In fact, the $CaMoO_4$ calculations proved to be a strenuous test case for the PAW method and this project contributed significantly to the development of the *pwpaw* code.
[30] P. E. Blöchl, Phys. Rev. B **50**, 17953 (1994).
[31] J. P. Perdew and Y. Wang, Phys. Rev. B **45**, 13244

(1992).
[32] N. A. W. Holzwarth, A. R. Tackett, and G. E. Matthews, Computer Physics Communications **135**, 329 (2001).
[33] C. L. Fu and K. M. Ho, Phys. Rev. B **28**, 5480 (1983).
[34] G. Herzberg, *Molecular Spectra and Molecular Structure* (D. Van Nostrand Company, Inc., 1950).
[35] N. A. W. Holzwarth and Y. Zeng, Phys. Rev. B **49**, 2351 (1994).
[36] C. E. Moore, *Atomic Energy Levels* (Superintendent of Documents, U. S. Government Printing Office, 1971), NSRDS-NBS 35 – National Standard Reference Data Series, National Bureau of Standards, Washington, DC, SD Catalog No. C13.48:35/V.I.
[37] O. K. Andersen, Phys. Rev. B **12**, 3060 (1975).
[38] This k-point sampling corresponds to that used in Ref. 23. The decision to use a smaller number of **k**-points for the $CaMoO_4$ simulations compared with those of $PbWO_4$ was made in order to save computer time. It can be somewhat justified on the basis of narrower, less dispersive bands. From our experience with these materials, we expect that the qualitative conclusions are are insensitive to this choice.
[39] In reference 23 the partial density of states were incorrectly reduced by a factor of 2. We would like to thank Dr. Peter Blaha for this correction.
[40] N. A. W. Holzwarth, G. E. Matthews, R. B. Dunning, A. R. Tackett, and Y. Zeng, Phys. Rev. B **55**, 2005 (1997).
[41] N. A. W. Holzwarth, G. E. Matthews, A. R. Tackett, and R. B. Dunning, Phys. Rev. B **57**, 11827 (1998).
[42] C. A. Daul, K. G. Doclo, and A. C. Stückl, in *Recent Advances in Density Functional Methods Part II*, edited by D. P. Chong (World Scientific, 1997), chap. 4, pp. 61–113.
[43] A. E. Hughes and B. Henderson, in *Point Defects in Solids*, edited by J. James H. Crawford and L. M. Slifkin (Plenum Press, 1972), vol. 1, chap. 7.
[44] Q. S. Wang and N. A. W. Holzwarth, Phys. Rev. B **41**, 3211 (1990).
[45] E. Scorza, U. Birkenheuer, and C. Pisani, J. Chem. Phys. **107**, 9645 (1997).
[46] W. B. Fowler, ed., *Physics of Color Centers* (Academic Press, 1968).
[47] A. Annenkov, E. Auffray, A. Borisevich, M. Korzhik, P. Lecoq, and V. Ligun, Nuclear Instruments and Methods in Physics Research A **426**, 486 (1999).
[48] R. T. Williams, Y. C. Zhang, Y. Abraham, and N. A. W. Holzwarth, in *SCINT99 – Proceedings of The Fifth International Conference on Inorganic Scintillators and Their Applications*, edited by V. Mikhailin (Moscow State University, 119899 Moscow, Russia, 2000), pp. 118–127, August 16-20, 1999, ISBN 5-8279-0007-9.
[49] V. V. Laguta, J. Rosa, M. I. Zaritskii, M. Nikl, and Y. Usuki, J. Phys.: Condens. Matter **10**, 7293 (1998).
[50] V. V. Laguta, M. Martini, F. Meinardi, A. Vedda, A. Hofstaetter, B. K. Meyer, M. Nikl, E. Mihóková, J. Rosa, and Y. Usuki, Phys. Rev. B **62**, 10109 (2000).
[51] M. Nikl, K. Nitsch, K. Polak, E. Mihokova, I. Dafinei, E. Auffray, P. Lecoq, P. Reiche, R. Uecker, and G. P. Pazzi, Phys. Stat. Sol. (b) **195**, 311 (1996).
[52] Q. Lin, X. Feng, and Z. Man, Phys. Rev. B **63**, 134105 (2001).
[53] H. A. Jahn and E. Teller, Proc. Roy. Soc. (London) **A161**, 220 (1937).
[54] V. V. Laguta, M. Martini, A. Vedda, M. Nikl, E. Mihóková, P. Boháček, J. Rosa, A. Hofstätter, B. K. Meyer, and Y. Usuki, Phys. Rev. B **64** (2001).
[55] M. Nikl, private communication.